Advanced Powder Technology 28 (2017) 325–339

Contents lists available at ScienceDirect

Advanced Powder Technology

journal homepage: www.elsevier.com/locate/apt

Review paper

3D analytical mathematical models of random star-shape particles via a combination of X-ray computed microtomography and spherical harmonic analysis ☆

E.J. Garboczi [a,*], J.W. Bullard [b]

[a] Applied Chemicals and Materials Division, National Institute of Standards and Technology, Boulder, CO 80305, United States
[b] Materials and Structural Systems Division, National Institute of Standards and Technology, Gaithersburg, MD 20899, United States

ARTICLE INFO

Article history:
Received 28 July 2016
Received in revised form 3 October 2016
Accepted 11 October 2016
Available online 27 October 2016

Keywords:
Particle shape
Spherical harmonics
X-ray computed tomography
Star shape
Shape parameters
Random

ABSTRACT

To compute any physical quantity for a random particle, one needs to know the mathematical shape of the particle. For regular particles like spheres and ellipsoids, the mathematics are straightforward. For random particles, with realistic shapes, mathematically characterizing the shape had not been generally done. But since about the year 2002, a method has been developed that combines X-ray computed tomography and spherical harmonic analysis to give analytical, differentiable mathematical functions for the three-dimensional shape of star-shape particles, which are a wide class of particles covering most industrial particles of interest, ranging from micrometer scale to millimeter scale particles. This review article describes how this is done, in some detail, and then gives examples of applications of this method, including a contact function that is suitable for these random shape particles. The purpose of this article is to make these ideas widely available for the general powder researcher who knows that particle shape is important to his/her applications, and especially for those researchers who are just starting out in their particle science and technology careers.

Contents

☆ Open Access for this article was sponsored by the Society of Powder Technology, Japan, through the Grant-in-Aid for Publication of Scientific Research Results, Japan Society for the Promotion of Science, 2016.

* Corresponding author.
E-mail address: edward.garboczi@nist.gov (E.J. Garboczi).

http://dx.doi.org/10.1016/j.apt.2016.10.014
0921-8831/

1. Introduction and motivation

There are many scientific areas and industrial applications where random-shaped particles play a critical role. "Random shape" can mean particles that are close to being spherical, with some random degree of shape perturbation, or collections of ellipsoids with a random distribution of semi-axes, or truly random particles, such as crushed gravel or sand, with shapes that are quite far from spheres or ellipsoids. In most of these cases, the actual shape of the particle plays a vital role in the properties being considered [1–3]. Examples include the packing of particles in a bed, the effect of inclusions on the rheological properties of suspensions, the effect on composite properties of inclusions embedded in a solid, and the light scattering from a particle. Microstructures that are built up in some way from a particle basis also depend on the shape or shape distribution of the original particles [4,5]. Another vital role is played by the particle size. For a sphere, the size is well-defined by the diameter. For a non-spherical regular object, the size can be described by a maximum length or by some weighted average of lengths across the shape. For irregular objects, this article shows that the particle size is not independent from the particle shape, so that any definitions of size will involve some analysis of the shape.

For regular particles, exact calculations such as light scattering, or indeed any integrals over the surface and volume, can be done since the volume and surface points are known analytically. For instance, taking the center of a sphere as the origin, the surface can be specified by the function $r(\theta, \phi) = R$, where θ and ϕ are the spherical polar angles and R is the radius of the sphere, and $r(\theta, \phi) \leqslant R$ specifies the volume as well as the surface. A triaxial ellipsoid centered on the origin is described by Eq. (1):

$$\frac{x^2}{a^2} + \frac{y^2}{b^2} + \frac{z^2}{c^2} \leqslant 1 \tag{1}$$

where a, b, and c are the semi-axes of the ellipsoid. Using spherical polar coordinates, the surface and volume of the ellipsoid are specified by

$$r(\theta, \varphi) \leqslant abc\left[(bc\sin(\theta)\cos(\varphi))^2 + (ac\sin(\theta)\sin(\varphi))^2 + (ab\cos(\theta))^2\right]^{-1/2} \tag{2}$$

The purpose of this review is to briefly describe how explicit, mathematical functions that can be differentiated at least twice, and which analytically specify the surface and volume of the particle, can be generated for a large class of random three-dimensional (3D) particles. This enables any calculation that can be done for geometrically regular particles can also be carried out for this class of random shape particles, denoted star-shape particles [6].

Many regular particles, such as spheres, ellipsoids, cubes, rectangular parallelepipeds (boxes), or pyramids, and simple variations thereof, are convex, which means that all the points on the line segment between any two points of the particle also belong to the particle. But many regular objects, such as golf balls, are not convex, and most irregular objects are not convex, either. A very large class of non-convex particles, which contains most particles used in industrial processes, particles dug up from the ground, and some biological particles found in human beings, is the class of star-shaped particles. An object is star-shaped if there is a fixed point, in its interior, for which a straight line drawn from that point to any other point inside the object lies entirely within the object. This is a relaxation of the convexity condition, with only one of the two points being arbitrary and the second point fixed. If we think of the fixed point as a coordinate origin, then a particle being star-shaped is the same as saying the surface is single-valued. The collection of all such fixed starting points itself forms a convex subset of the object and is often called the kernel of the star-shaped object [7]. The star-shaped requirement will exclude from consideration particles with overhangs or internal voids. Overhangs mostly become knocked off in most natural and industrial processes, but can stay on in biological processes, which are usually much less energetic. Particles having internal voids are found more commonly in industrial and natural processes. However, the internal voids can be filled in, so that the particle becomes star-shaped and the outer surface can then be analyzed.

This review article will describe a measurement and analysis technique for star-shaped particles that results in an analytical approximation for a particle's shape, from which any geometrical quantity can be determined for the particle via surface or volume integration. The surface is at least twice differentiable, so that surface curvature can also be computed. Any calculation that employs such particles, for example light scattering from the particle surface or the moment of inertia tensor calculated over the volume, can be carried out in the same manner as for spheres or ellipsoids.

2. X-ray tomography of powders

To be able to fit a spherical harmonic (SH) expansion to the surface of a particle, a 3D image of the particle is first needed. The way we have chosen to obtain this image is via X-ray computed microtomography (CT). For particles above about 3 mm to 10 mm in size, one can pack an X-ray transparent container with particles, using some kind of polymeric foam spacer between the particles to keep them from touching in either the container or in the eventual X-ray CT image. The assumption is that there is significant contrast between the polymer foam and the particles so that they can be distinguished in the CT images. The packing must be mechanically stable, for any viscoelastic relaxation in the spacing material or other shift in the particles, in the time frame of the measurement, will blur the images. On the X-ray CT images, this foam material will typically appear very dark compared to the particles, and so will be easy to remove using image analysis. The container is then mounted on some kind of sample stage – we have used a small amount of clay to temporarily "glue" the container on to a flat sam-

ple stage, for example. The container is scanned and the images segmented and stacked together to form a 3D block of integer data (e.g., 1 = particle, 2 = background).

For particles smaller than about 3 mm, a simple technique is to embed the particles in an epoxy inside some kind of tube. Again, the main idea is to physically separate the particles so that they are not touching in the sample or in the CT images. We have found that a volume fraction of 10% or less is adequate for particle separation. For most particles we have examined, simple hand stirring of powder added to liquid epoxy is adequate for dispersing the particles. For particles larger than about 500 μm, the particles have a tendency to settle while the epoxy cures and perhaps touch in the sample. This settling can be prevented in two ways. The first is to stir the liquid/powder sample until the viscosity increases enough in the curing process so that the particles no longer settle. Another way is to put the samples on some kind of rotating platform, timed to rotate so that the particles are not able to settle into one place under gravity but the direction of settling is constantly being changed. For smaller particles, down to 1 μm or so, settling has never been an issue. More details on the sample preparation process are in Ref. [8]. For particles in the 0.5–3 mm range, often the particles can be spread out on an adhesive polymer sheet and then rolled into a cylinder suitable for scanning.

The result of the X-ray CT process is a series of cross-sectional slices, taken across the vertical direction, of the particles embedded in epoxy or some other medium. A typical number is 1000 images, where each image is 1000 × 1000 pixels in size, and either 8 bit or 16 bit per pixel. These images then need to be segmented into two-phase images, so that the particles are white and the matrix is black. When using an interior scan on an instrument like the NIST Zeiss Versa XRM500,[1] where only an interior portion of the sample is reconstructed, a technique known variously as interior or region of interest or local area or local scanning [9,10], each reconstructed image is perfectly circular. In this case, particles that touch the circle boundary could have been artificially cut and so should be discarded. A third phase, at some intermediate gray scale, should be created around the outside of the circle and inside the complete square image, so that particles that touch this phase can be discarded. The pixel size is always given in the X-ray CT process, and needs to be preserved for the step in Section 4.

3. Description of computer algorithms used to extract and analyze particles

After applying a threshold, the slices are stacked together using a program that reads in each image and converts it to ascii (tiff2array.c). This is a simple but crucial step in changing the image data into a data structure that can be processed by further particle generation programs. The final result is a 3D array with integer values corresponding to each phase. A variation of this procedure can be made so that the image stacking and ascii conversion is done first and then the thresholding is done in 3D. When an interior scan has been made so that there is an artificial circular boundary in each image, a slightly different procedure is used (tiff2pgm2mic.f) to generate the asci image stack.

Special software was written in Fortran 77 to extract the particles (part-proc.f). The software looks for voxels of a certain phase number, which indicates a particle. Once a particle is found, then all voxels with the same label that are connected to the first voxel are subsequently identified using a burning algorithm [11]. When no more such voxels are found, then the collection of voxels found is identified as a particle. During this process, an indicator is turned on if one of the voxels contacted a surface, either of the images themselves or, if there is a third phase surrounding the cylinder of real data, contacting this third phase. Either case indicates a particle that has possibly been artificially cut and so should not be further considered. If the indicator variable is turned on, the voxels of the particle found are erased from the array. A simple check for possible double particles is also done at this point. An artificial double particle would be two particles that were close together, but not touching, in the original sample that have been apparently connected in the image reconstruction process. In this case, the center of mass of the double particles could lie outside the boundaries of the particle. If this is the case, these voxels are erased from the particle array. If the collection of voxels identifying a particle survives these two tests, it is then ready to be analyzed in terms of spherical harmonics. Similar X-ray CT work, followed by shape analysis but not spherical harmonic analysis, has been done for actual lunar soil [12,13] and lunar soil simulants [14,15].

4. Spherical harmonic (SH) expansion

4.1. Particle restrictions and SH analysis

A particle that has some internal porosity, or has a few internal non-particle voxels generated during the thresholding process, is examined and these voxels are turned back into particle voxels in the part-proc.f program. The particle then does not have any holes in it. An object that does not have any holes in it and is star-shaped can be analytically described by the function $r(\theta, \phi)$, introduced in Section 1 of this review, where $r(\theta, \phi)$ is the distance from the origin, taken inside in the particle in the kernel (see above), in the (θ, ϕ) direction. The usual spherical polar coordinate system is used, where θ is the angle from the positive z-axis, and ϕ is the angle from the positive x-axis, taken to be positive in the counter-clockwise direction. The function $r(\theta, \phi)$ is said to be defined on the unit sphere [16].

Such a function like $r(\theta, \phi)$ can be approximated as a truncated SH series [16],

$$r(\theta, \phi) \approx \sum_{n=0}^{N} \sum_{m=-n}^{n} a_{nm} Y_{nm}(\theta, \phi) \tag{3}$$

with the approximation being exact in the limit $N \to \infty$. For all particles considered so far by this technique, the maximum value of N is typically around 30.

The collection of voxels that define a particle is then analyzed using Eq. (3). The center of mass is found and used as the origin, assuming it lies within the kernel of the particle, which is almost always the case for star-shape particles, and a Gaussian quadrature is defined for both θ and ϕ. Experience has shown that a 120 point Gaussian quadrature is sufficient for both these angles. At each pair of angles, $120^2 = 14{,}400$ pairs, $r(\theta, \phi)$ is numerically determined using the digital surface and the pixel size, so that the units of $r(\theta, \phi)$ are in the real particle units, not numbers of voxels, making use of the physical length per voxel recorded in the X-ray CT scan. Pairs of points are chosen along the given direction, and it is determined whether or not they bracket the surface. When they do, a closer pair of points is chosen and so on, down to a given minimum cutoff value, which identifies the exact point where the ray from the origin crosses the particle surface.

The spherical harmonic functions are orthonormal. Therefore, the coefficients of Eq. (3), a_{nm}, can be determined by the following integral:

$$a_{nm} = \int_0^{2\pi} \int_0^{\pi} d\phi d\theta \sin(\theta) r(\theta, \phi) Y_{nm}^*(\theta, \phi) \tag{4}$$

[1] Commercial equipment, instruments, and materials mentioned in this paper are identified in order to foster understanding. Such identification does not imply recommendation or endorsement by the National Institute of Standards and Technology (NIST), nor does it imply that the materials or equipment identified are necessarily the best available for the purpose.

where the asterisk indicates a complex conjugate. Since the angles were chosen according to Gaussian quadratures, it is easy to do the integral in Eq. (4) numerically, since the $r(\theta, \phi)$ function was analyzed at the Gaussian quadrature points. The integral in Eq. (4) in practice always readily converges, and the real and imaginary values of the a_{nm} coefficients decrease steadily with increasing values of n. Evaluating Eq. (4) gives the values of a_{nm} for $0 \leqslant n \leqslant N$ and $-n \leqslant m \leqslant n$. In the same program, an additional error check is made. The number of voxels defining a given particle is known, and the pixel or voxel length scale is known, so that the volume of the particles in real length units is easily computed. The SH expansion, which defines the functional form of $r(\theta, \phi)$, can be used to directly calculate the volume of the particle via

$$V = \frac{1}{3}\int_0^{2\pi}\int_0^{\pi} d\phi d\theta \sin(\theta) r^3(\theta, \phi) \tag{5}$$

This volume is compared to the voxel-based volume. If the difference is less than a user-defined value, usually 3–5%, then the particle is considered to be faithfully rendered with the SH expansion. The SH coefficients are put into a file, which is named with a root string corresponding to the type of particle being studied, followed by the number assigned to the particle. If the volume difference is larger than the cutoff, then the particle is discarded and its number is given to the next good particle. At this point, discarding a particle due to its failing of this test is most likely because the particle was a double particle of some kind, so that it had pieces of its outline that could not be described by a star-shaped particle. As a final step for a good particle, a Virtual Reality Modeling Language (VRML) image [17] is made directly from the SH coefficients and stored with the same root string and particle number. This is a simple graphics image format that has been superseded by the X3D standard [17]. VRML is based on an STL-compatible listing of the polygons making up the surface, along with some rendering commands, and is easily convertible to other popular formats, including X3D.

In a sense, this technique generates something like a "point cloud" on the surface of a given particle. In the literature, there are other ways of generating a differentiable, single mathematical function that fits the point cloud. A popular mathematical method is using radial basis functions [18–20], which has tended to be applied more to macroscopic objects rather than microscopic powders. However, it is applicable to non-star-shaped objects, which would make it more general than the spherical harmonic approach described in this article. But for application to thousands of small powder particles, the spherical harmonic approach may be computationally simpler and faster.

4.2. Computation of various geometrical quantities

After a list of particles is extracted from the processed X-ray CT data array, another program (part-lwt.f) operates on this list. The parallel form (written in MPI) of this program breaks the list up into pieces that are worked on by each processor. This program reads in the SH coefficient files, and computes a number of geometrical quantities for each particle, using $N = 2, 4, 6, 8, \ldots$ One of the geometrical quantities computed is the Gaussian curvature, integrated over the surface of the particles as defined by $r(\theta, \phi)$ [11]. For a closed object, one with no holes in it, the integrated Gaussian quadrature must be equal to 4π. This fact is used as another error analysis step. As N gets larger, the SH functions can probe smaller and smaller "ripples" in the particle surface. N has no upper limit, but the size of the "ripples" in the particle surface is limited by the voxel size. Therefore, the agreement between the computed integrated Gaussian curvature and the theoretical value of 4π is used to choose when N is large enough. If the error in the integrated Gaussian curvature values becomes larger than 5% (or any other user-defined tolerance), then the SH series is terminated and the maximum value of N for that particle, N_{max}, at which the agreement was better than 5%, is stored. All future uses of that particle, to be accurate, must use the stored value of N_{max}. If N_{max} is less than 14, then that particle is discarded, since we only want particles whose shape is known to at least $N_{max} = 14$. The final value of the integrated Gaussian quadrature is stored.

For each good particle, the following information is also stored. First, the extents of the particle are computed. These are the minimum and maximum x, y, and z coordinates found on the particle's surface. These determine a box, called the Extent Box [21], which just surrounds the particle and touches it at only six points. The Extent Box is determined for the arbitrary orientation that the particle had in the original X-ray CT sample. Then the volume and surface area are computed, with the surface area S defined by

$$S = \int_0^{2\pi}\int_0^{\pi} d\phi d\theta r(\theta, \phi)\left[r_\phi^2(\theta, \phi) + r_\theta^2(\theta, \phi)\sin^2(\theta) + r^2(\theta, \phi)\right]^{1/2} \tag{6}$$

where the subscripts in Eq. (6) indicate partial differentiation with respect to the variable listed. The volume equivalent spherical diameter is computed, which is the diameter of a sphere with the same volume as the particle. The surface area of this sphere is also computed, and is used to normalize the actual particle surface area, for which the ratio is stored separately.

The moment of inertia tensor, assuming a constant density, is computed and stored, along with its trace, which is normalized by the trace of the moment of inertia of the volume equivalent sphere just defined. Another kind of curvature, the mean curvature [11], is integrated over a particle's surface. It can be inverted and normalized so that the integrated mean curvature for a sphere would be equal to the diameter. This is another equivalent "size" for the particle. For spheres, it is exactly equal to the volume equivalent spherical diameter, but as a particle becomes less spherical, these two values increasingly differ. The ratio between the two lengths can then serve as a measure of sphericity. Finally, the length (L), width (W), and thickness (T) are computed for each particle and stored [22]. L is defined as the longest surface point to surface point distance on the particle. W and T are defined similarly, except that W must be perpendicular to L and T must be perpendicular to both L and W. This set of three lengths is another way of defining a box that just fits the particle, similar to the Extent Box but with edges aligned along L, W, and T, which are mutually perpendicular. L, W, and T are quite similar numerically but are not defined in exactly the same way as the usual way sedimentary geologists define three lengths per particle (D_1, D_2, D_3) [23]. The values of L, W, and T, as well as their values normalized by T, are stored for each particle. The ratios L/W and W/T can serve as approximate aspect ratios for each particle, and their distribution is a measure of the shape distribution for a given class of particles. These values are stored in a file that usually has the root name of the particles followed by the extension ".geo." Certain geometrical factors can be looked for in this file, say particles having a large value of L/T, and then their 3D VRML images can be viewed, since the numbering on the particles remains consistent. Other shape-related quantities, such as convexity and the maximum radius inscribed sphere and the minimum radius circumscribed sphere, can be generated using TSQUARE (see Section 7).

4.3. Corrections

A well-known artifact introduced by truncated SH series representations is the Gibbs phenomenon, or "ringing"—the appearance of small, high-frequency ripples on the surface and especially near

the poles. The ripples near the poles are probably at least partially an artifact of the Gaussian quadrature scheme used for the numerical values of θ and ϕ used, which tend to over-sample near the maximum and minimum values of θ. However, a common technique for reducing the ringing artifact, without significantly affecting the overall shape, is to filter the series with the so-called Lanczos sigma factor [23,24], by which each of the SH coefficients are transformed according to

$$a'_{nm} = a_{nm}\mathrm{sinc}\left(\frac{(n-n_0)\pi}{N-n_0}\right), \quad (n_0 \leqslant n \leqslant N) \tag{7}$$

where $\mathrm{sinc}(x) \equiv (\sin x)/x$ and n_o is the degree below which the coefficients remain unchanged and N is the cutoff defined in Eq. (3). The Lanczos sigma factor progressively reduces the magnitude of the SH coefficients as n approaches N. When calculating principal curvatures on a particle surface, the ringing artifact can significantly affect the results; artificial ripples produced by truncating the SH series can have appreciable curvatures even though their amplitude is small. However, the effect of ringing and its correction has little effect on the volume and surface area calculations. Although the calculated curvatures of a simple rounded particle such as an ellipsoid can be influenced considerably by ringing artifacts when they are not dampened by the sigma factor, the effects are even more pronounced on particles with large flat areas, such as the faces of a cube. The ringing artifacts in these last examples are somewhat analogous in scale to the texture or surface roughness of real-shaped rock and powder particles. Both texture information and ringing are contained in the higher-frequency terms of the SH expansion, so numerical methods for reducing ringing will also tend to smooth out the particle's real texture. The distribution of principal curvatures on the surface of star-shaped particles also can be calculated from the SH series approximation of the shape. Both artificial ringing, due to the truncation of the SH series, and real texture of the particle surface, can introduce considerable noise in the distribution of curvatures. This noise can be reduced significantly by application of Lanczos's sigma factor, although again at the probable price of removing some real surface detail along with the noise.

This same particle identification and SH procedure can operate on point clouds generated using laser range finding [25] or any other technique on particles. The point cloud is interpolated to a grid of points where the spherical polar angles are distributed according to a Gaussian quadrature, as was described above. Then the SH coefficients are generated the same way and the rest of the analysis follows. It should be noted that all the computer programs mentioned in this review article, including TSQUARE, will be made available at ftp://ftp.nist.gov/pub/bfrl/garbocz/.

5. Overlap algorithm and 3D many-particle models

There are many models of particles where particle contact plays an important role. These include various random packing and placement models [26,27] and of course all discrete element method models, which are growing in popularity and application [28]. The question of whether two spherical particles overlap is easy to answer – compare the center-to-center distance to the sum of the two sphere's radii. If the center-to-center distance is less than the sum of the radii, then the spheres must overlap. Ellipsoids are harder mathematically, but there are also analytical formulae that will determine overlap for ellipsoids of revolution and triaxial ellipsoids [29,30]. The key to having an analytical contact or overlap function for spheres and ellipsoids is knowing their surfaces analytically. Since, for a random, star-shaped particle, the SH series gives us an analytical form for $r(\theta, \phi)$, it should be possible to develop a contact function for these kinds of particles. This has been done [21] for an arbitrary pair of SH particles, though it is not in an analytical form, due to the complicated nature of Eq. (3). The algorithm makes use of the Extent Overlap Box (EOB), which is defined by the intersection of the Extent Boxes from the two particles. If this intersection is empty, then the two particles cannot overlap or contact each other. If the EOB exists, then the two particles might overlap. Both particles could not touch the EOB, or only one of the two, in which case no overlap can exist. If both particles extend inside the EOB, then only those small sections of the particles can be efficiently numerically checked for overlap. Using the EOB greatly increases the efficiency of the algorithm.

Using an earlier version of this contact algorithm, a model has been constructed, called the Anm model, which randomly places SH particles into a unit cell using either fixed or periodic boundary conditions [31]. Each particle is chosen from a given dataset, from a specific size range, and is randomly rotated before attempted placement in the unit cell without contacting any other particles. In this way, cement or mortar or concrete microstructures can be developed. Adaptive finite element meshes can be generated to fit this microstructure and compute properties [32]. The above contact algorithm [21] has been incorporated into the Anm model, along with allowing each particle to have one or more uniform thickness interfacial zones around its surface [33]. This enables a quantitative study to be made of processes that are dependent on distance from a particle surface. In addition, a degree of parallelism has been built into the model, greatly improving its speed on multi-processor systems [33]. The Anm model has been applied [34] to study the interfacial transition zones [35] around sand and gravel particles in mortar and concrete, showing the comparison between 2D and 3D microstructure imaging of these thin zones, which are important in helping determine mortar and concrete transport properties [35].

6. Applications

This section briefly describes a number of applications of the combined X-ray CT/SH particle analysis. It is important to remember that each such application adds to a database of particle shapes for various particle types. This database, stored at NIST, now contains several million particles.

6.1. Virtual sand and rocks

The initial driving force for shape characterization of gravel and sand was for application to multi-scale concrete models, embodied in the Virtual Cement and Concrete Testing Laboratory [36]. The desire was to use realistic particle shapes, since for certain properties, particle shape mattered significantly. One of these was early age mortar (sand plus cement and water) and concrete (mortar plus gravel) rheology, before a mixture hardened, since particle shape is known to play a large role in suspension rheology or viscosity [37]. After concrete has set, but before much hardening and stiffening has taken place, early age elasticity is dependent on sand and rock shape, since at early ages after mixing, there is a large contrast between the elastic moduli of the sand and rock inclusions and the cement/water matrix. When the elastic contrast is large, particle shape, for geometrically regular and irregular particles represented by SH series, is known to significantly affect composite properties [38].

Images of three Ottawa sand grains, a 100% pure silica sand often used in various US and international mortar and concrete standards, are shown in Fig. 1. Similar sands are used in other countries, including Toyoura sand in Japan [39] and Leighton-Buzzard sand [40] in the UK. The images are a VRML rendering of the SH representation of the particle that was derived from an X-

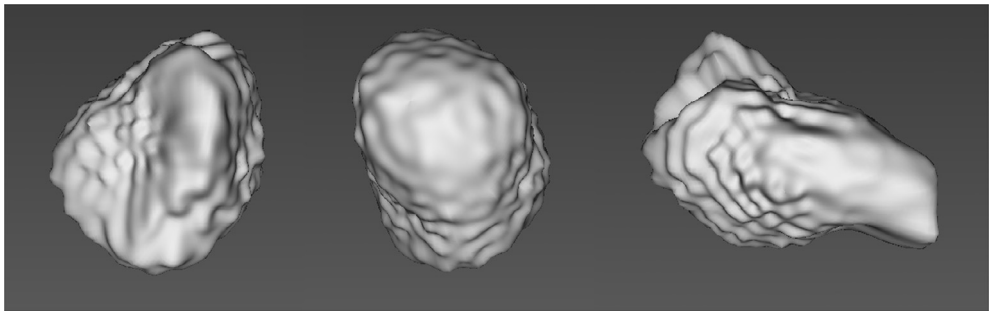

Fig. 1. VRML images of Ottawa sand particles. Each image is about 0.25 mm in size.

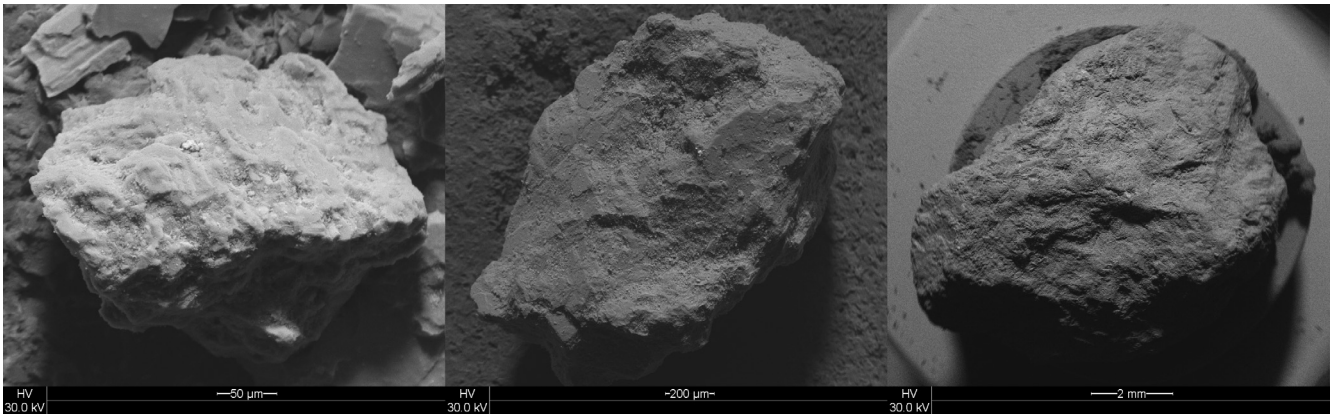

Fig. 2. Showing particles from the Small (left, image width = 360 µm), Medium (middle, image width = 1.8 mm), and Large (right, image width = 11 mm) size ranges, with magnifications chosen so that they all appear to be about the same size.

ray CT scan. The surface may contain some "digital roughness," which means some aspect of the original voxel surface has been reproduced by the SH analysis. By reducing the number of SH functions used, some of this digital roughness may be reduced, which will also tend to partially reduce any real roughness in the surface at the voxel scale. These particles can be easily used in various 3D models of mortar and concrete, such as the Anm model mentioned earlier [31,33], along with images of larger gravel particles.

6.2. Size vs. shape of rocks

Since most rock and sand for concrete, asphalt, and gravel bed support come from blasted and crushed rock, a study was made of rock of a single type that had been blasted and crushed. The size scale ranged from 60 mm down to about 20 µm, a range of 3000 in size [41], as defined by standard sieve analysis. The particles were divided up into three size ranges: Small = 0.0175–0.24 mm, Medium = 0.24–3.29 mm, and Large = 3.29–45.1 mm. Each size range covered about 1.1 decade in the width parameter, which was taken as a reasonable measure of particle size. Fig. 2 shows three scanning electron microscope (SEM) images of one particle from each of the three size ranges, with the magnification chosen to make each particle appear to be about the same size. There are no particular qualitative differences between the three rocks, which makes any potential scale-invariance of the shape parameters seem more plausible.

Various shape parameters were computed for all the 58,000 particles, and statistical distributions were constructed for the three size ranges. One shape parameter that was used was defined from the mean curvature, κ [42,43], defined at a surface point, integrated over the particle surface as reconstructed by the spherical harmonic series and normalized by the surface area. This integrated parameter, defined as K, is size dependent, since it has units of reciprocal length. If it is multiplied by the volume equivalent spherical diameter (VESD) size parameter, where the value of VESD for an arbitrary particle is defined as the diameter of a sphere with volume equal to the particle, this ratio becomes a dimensionless, size-independent shape parameter. There are different normalizations for the mean curvature. We choose the normalization so that for a sphere, $K = 1/R$, which is a constant for a sphere and where R is the radius of the sphere. Therefore, twice the inverse of the integrated mean curvature would give the diameter for a sphere, so that normalizing by the *VESD* would give unity for a sphere. Non-spherical objects will give a value less than one. We therefore define the shape parameter *CP* to be:

$$CP = \frac{2K^{-1}}{VESD} \tag{8}$$

Fig. 3 shows the statistical distribution of the *CP* shape parameter plotted over the three size ranges. It is clear that the particle shape, as defined by this particular shape functional, is similar for each size range, implying a degree of universality over a wide range of size scales for rock that was blasted and crushed. A similar result was found for the other shape parameters considered. In Fig. 3, note that the Large curve has more statistical noise in it than the other curves due to containing the least number of particles of all three size ranges.

6.3. 2D vs. 3D shape characterization of rocks

In the sand and gravel industry, there is awareness of the effect of particle shape on composite properties, but there is a lack of measurement techniques for 3D shape. This is true for most industries that manufacture powders of various size scales. For sand and

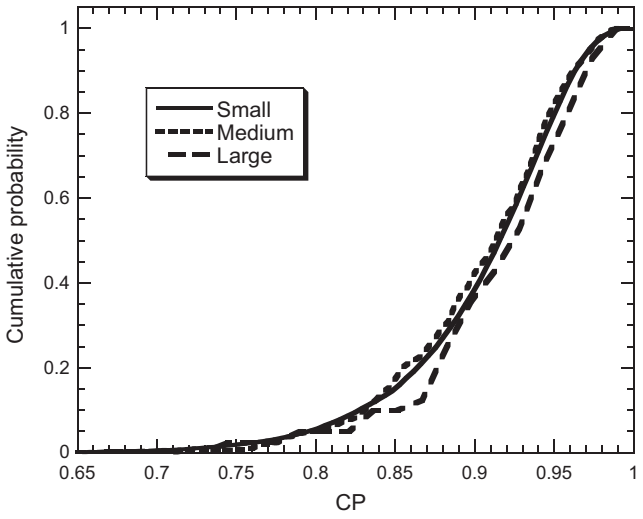

Fig. 3. The distribution of the shape functional CP, plotted for the three size subranges that together make up the entire particle size range studied.

gravel, a 2D method that is becoming popular is called the Aggregate Imaging System (AIMS) [44], and consists of laser scanning and digital images of gravel particles spread over a surface. Comparisons of the 2D results from this instrument have been made to 3D shape analysis from the X-ray CT/SH method [45,46], on the exact same rocks. The comparison showed that useful shape information can be obtained from the AIMS system, although some of the data is not the same as the true 3D information. The AIMS system gives some quasi-3D information in the dimension perpendicular to the surface upon which the particles are laid, but not complete 3D information. This is also true for those particle measurement systems that take rapid 2D projection images of particles falling past a camera [47].

6.4. ASTM particle shape draft standard

There is an ASTM standard, D4791-10 *Standard Test Method for Flat Particles, Elongated Particles, or Flat and Elongated Particles in Coarse Aggregate*, which essentially measures the length, width, and thickness for individual rocks. This measurement technique gives accurate information, but is tedious to perform and only is useful for gravel sizes greater than about 20 mm, as defined by standard sieving. A new draft standard is being worked on, using the X-ray CT/SH techniques, which will provide a standard way of measuring the shape, particularly the length, width, and thickness, for sand-size particles, from 3 mm down to 0.1 mm in size, again as defined by sieving [48].

6.5. Particle shape analysis of fine particles for concrete

A systematic study has been carried out of 10 Norwegian rock types, crushed in a vertical shaft impact (VSI) crusher and air-separated into three size ranges: 0–20 μm, 20–63 μm, and 63–125 μm. Epoxy samples were made and scanned in an X-ray CT. Several million particles were obtained and analyzed with these SH methods. The results are being presented in four articles to be published [47,49–51]. It was found that the VSI crusher tends to make particles more equi-axed [51] compared to the usual cone crushers. This can be determined for particles above a few millimeters in size, with standard techniques, but only the combination of X-ray CT and SH analysis was able to do this for hundreds of thousands of particles in the above three size ranges. Because of their high surface area to volume ratio, these small particles tend to have a large effect on the rheology of fresh concrete. It was also found that the average L/W and W/T ratios tended to be constant across one of the above size ranges, indicating the utility of using the average aspect ratios, rather than a full distribution, as simple parameters for determining shape-related uses of these small particles in cement-based systems [51]. The usual definition of the empirical shape parameter "flakiness" [52] for particles larger than 4 mm, measured by using special asymmetric sieves [53], was modified for these much smaller particles, using the shape parameter T/pW, and designated "microflakiness." If the value of T/W for a particle was such that $p < 0.564$, then the particle was classified as being flaky, in agreement with the usual flakiness sieves mathematically extended down to this smaller size range [51]. An algorithm was written to generate random 2D projections and 2D geometric quantities (e.g. perimeter, Feret diameters) from the 3D spherical harmonic particles. This enabled quantitative comparisons to be made, for the exact same particles, between 2D data as measured by optical imaging devices and 3D data generated mathematically from the actual particles [47].

6.6. Portland cement – shape and chemistry

The particle shape of Portland cement powder, which is the cement used in the vast majority of mortar and concrete used worldwide (on the order of 4 billion metric tons per year [54]), is important in many areas of concrete use [55] and is influenced by its mineral composition. This is because in the Portland cement manufacturing process, the multi-mineral phase material, called clinker, which is found after reacting calcium, silicate, and other minerals in a high-temperature kiln, is extensively ground in a ball mill. Certain mineral phases are harder than others, so that a cement powder with more of these phases will grind differently than a cement with less of these phases, resulting in a different average shape. This has been confirmed by a recent X-ray CT/SH study [56]. Shape in this case is measured by the value of L/W, averaged over all particles considered. In Ref. [56], about 3000 particles were considered for each of eight cements studied. A VRML image of each particle type is shown in Fig. 4.

While grinding is a complicated process, factors influencing grindability include hardness of the individual phases, internal porosity, crystal size, and defects such as microcracking. In addition, the fracture toughness of each phase as well as each phase's plasticity influences the response to the grinding process. The main component of Portland cement, alite ($Ca_3SiO_5 = C_3S$), which is formed at higher temperatures, exhibits fractures that appear like cleavage planes. Belite ($Ca_2SiO_4 = C_2S$) crystals, which are formed at lower temperatures, have a rounded habit and do not appear to have a tendency to cleave when ground. Cements with more alite and less belite are ground by breaking alite crystals, producing less equi-axed particles and larger average L/W values. Cements with more belite and less alite have less of a tendency to have broken particles, so will have a higher percentage of equi-axed particles and therefore average L/W values closer to unity. These characteristics help explain the results shown in Fig. 5, which show a roughly linear decrease in average aspect ratio as the amount of belite increases.

6.7. Size vs. shape for Portland cement

For a given cement, the grinding process results in a wide size range, from sub-μm particles to about 60 μm particles. Using focused ion beam (FIB) techniques to image particles from a few tenths of a micrometer up to 20 μm in size, and using the usual X-ray CT techniques for the larger particles, the shape distribution was compared between these two size ranges for a given cement and found to be almost identical [57]. However, the smaller FIB

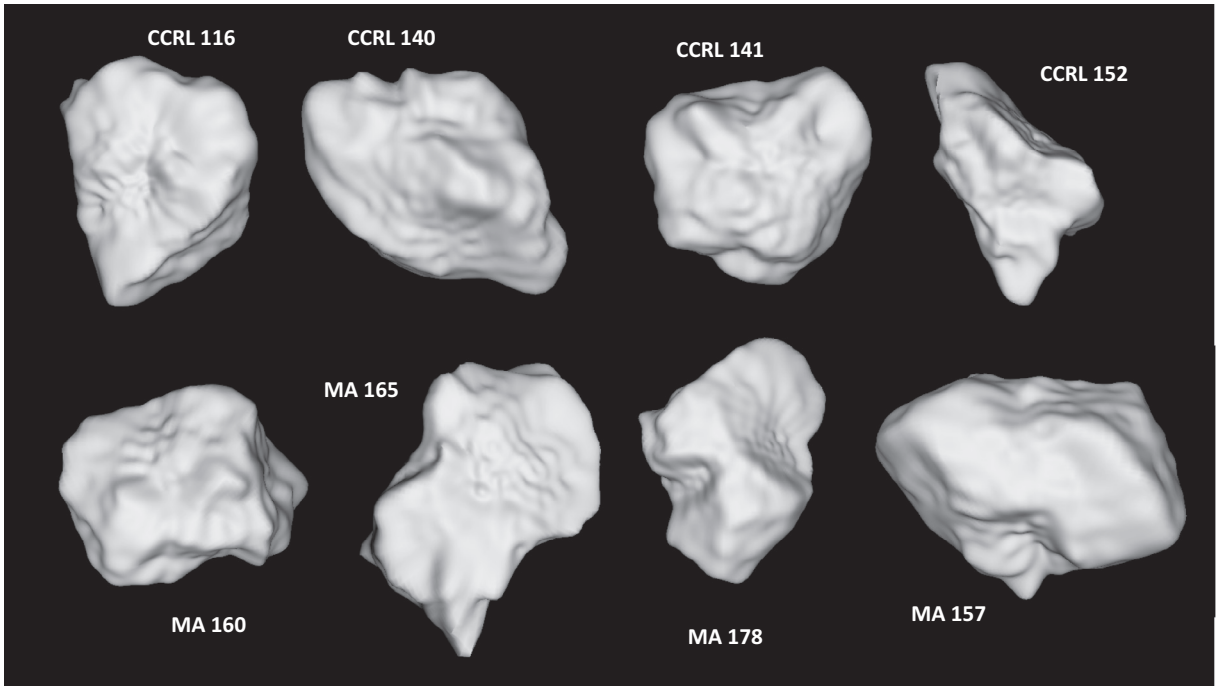

Fig. 4. A sampling of the eight different cements, showing the range of particle shapes available (not to scale).

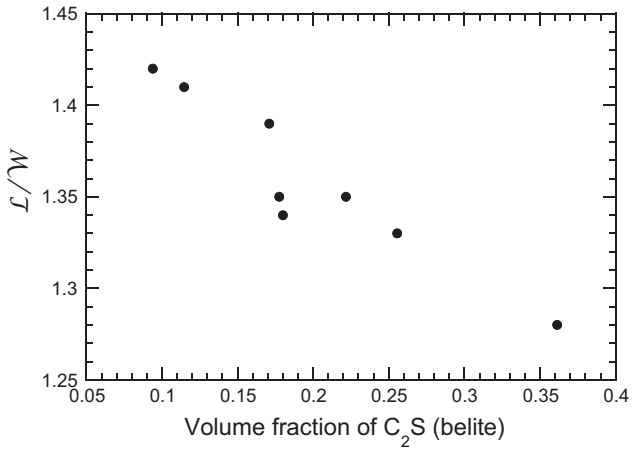

Fig. 5. The average value of L/W plotted vs. the volume fraction of belite, or $C_2S = Ca_2SiO_4$.

particles tended to be slightly more prolate than the larger CT particles, which might be expected for small "chips" knocked off larger particles. This can be qualitatively seen in Fig. 6 below, where the normalized width (W/T) distributions are essentially the same for the two size classes, while for the normalized length (L/T) distribution, the distribution for the smaller (FIB) particles are peaked at a slightly larger L/T value.

6.8. Effect of cement shape on hydration

Using a detailed model of cement hydration [58], 3D microstructures of cement paste (cement plus water) were compared for real-shaped particles of different sizes vs. spherical particles. Cement particle shape mainly matters at early reaction stages, where a larger surface area due to less-spherical particles can accelerate hydration. As the cement dissolves and is reacted away, at later time stages, the initial shape matters less. This type of behavior should be general for any reaction of powder with an enveloping fluid, where the particles are randomly consumed by the reaction.

6.9. Surface area of shredded automobile tires

For a sphere, or any other geometrically regular particle, it is simple to calculate the surface-area-to-volume ratio, sometimes called the specific surface area. For many particle applications, the specific surface area is an important parameter, as was seen for cement. A humble but important application is drain field/sewage systems, where biofilms grow on the surfaces of particles and play a key role in chemically reducing waste materials [59]. An estimate of the biofilm thickness, which is an important parameter in characterizing the effectiveness of the sewage/drain field system, comes from dividing the total biofilm volume, determined destructively on a set of particles, by the particle surface area. Common mathematical treatment assumes the particles can be modeled as spheres [60]. Fig. 7, showing four shredded tire particles out of those studied, shows that this is not a good assumption. When the particles used are very non-spherical, using a sphere approximation for the specific surface area can make biofilm thickness predictions in error by 100% or more. The X-ray CT/SH system was used to characterize the shapes, and therefore the specific surface area, of particles made from shredded automobile tires, which were intended to be used in a drain field/sewage system [61]. A quantitative estimate was obtained for the specific surface area of these irregular particles, which greatly improved the estimation of the biofilm thickness as compared to experimental results.

6.10. Roundness of glass beads

Glass beads are used as an additive to paints used for marking lines on road pavements. When a car headlight hits a glass bead, the light is reflected back (retroreflectivity) towards the driver, increasing the visibility of the pavement marking. The degree of

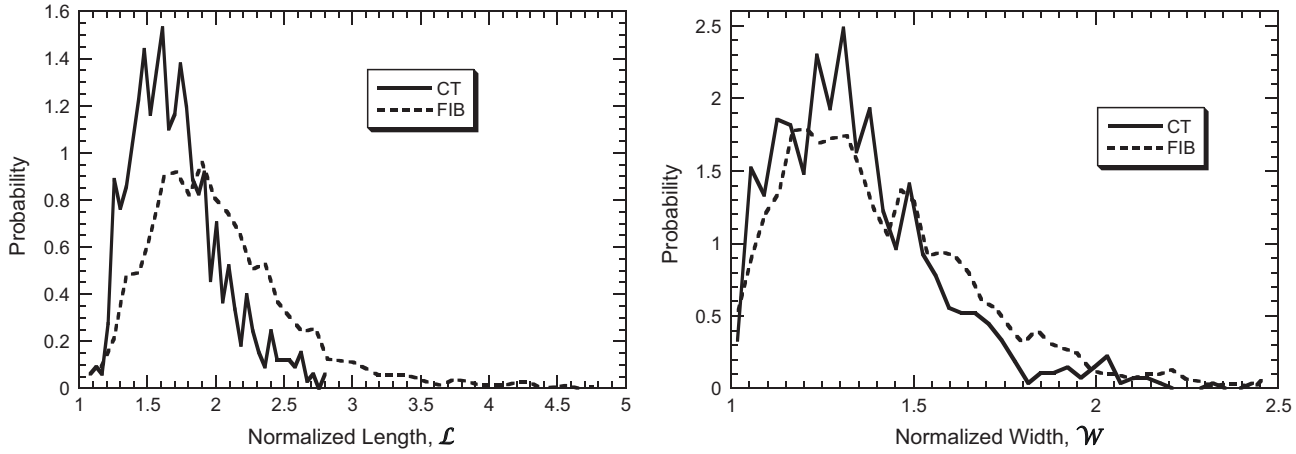

Fig. 6. L/T (left) and W/T (right) distributions for the smaller (FIB) and larger (CT) cement particles.

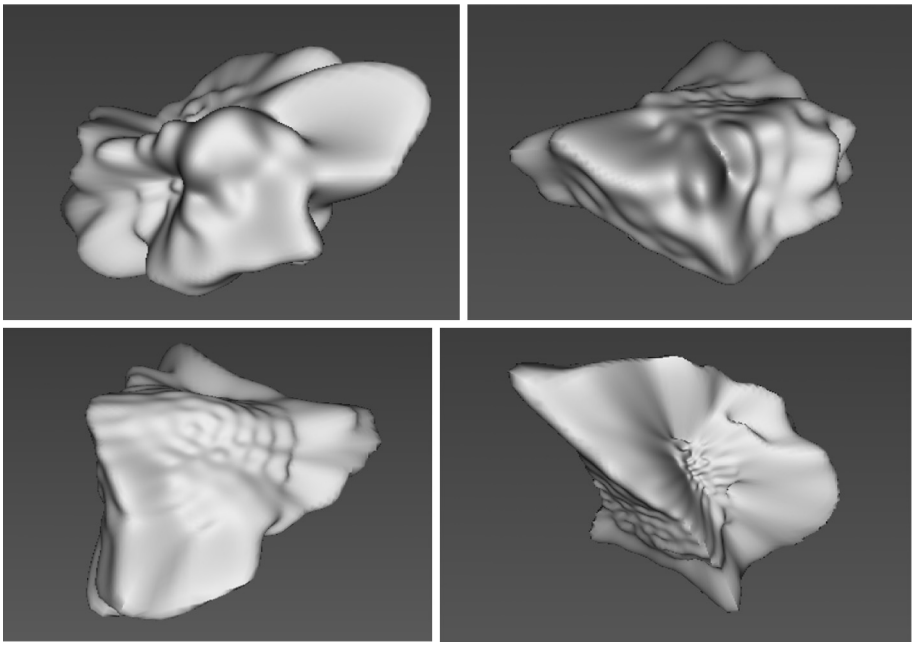

Fig. 7. VRML images of four particles, each between 5 mm and 10 mm in average linear dimension.

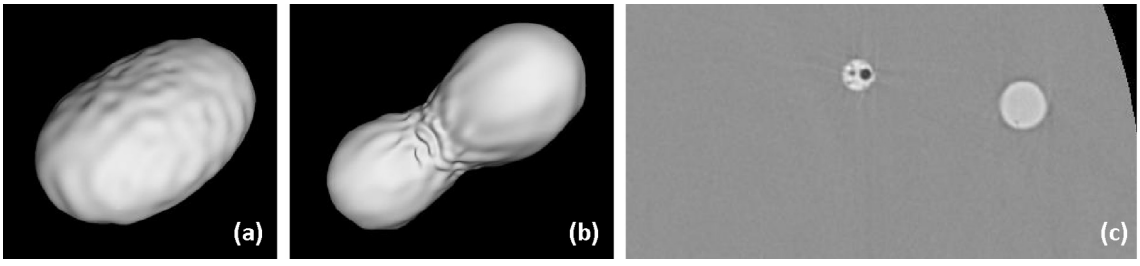

Fig. 8. (a and b) two typical non-spherical glass particles found in glass beads for pavement coatings, which were rejected by the mechanical shape device used by US state departments of transportation and (c) part of one X-ray CT slice of standard glass beads in epoxy, showing internal porosity left over from the manufacturing process.

retroreflectivity is controlled by the sphericity of the glass bead, with a greater degree of sphericity resulting in a higher amount of retroreflectivity. Since glass beads for pavement paint must be inexpensive, departments of transportation run various tests to measure the degree of sphericity of glass beads from various sources so as to determine their suitability to meet specifications for pavement paint. Glass beads are also manufactured, in more expensive processes, to serve as standards for light-scattering-based particle size measurement and other such higher-precision uses. A study was done comparing 3D X-ray CT/SH shape and size characterization to various methods commonly used for glass beads in pavement paint and glass spheres made as standard par-

ticles for laser diffraction particle size measurement [62]. Fig. 8a and b shows two glass beads manufactured for use in pavement marking paint. These are two beads that had been rejected by a machine used by US state departments of transportation that separates particles according to an empirical measure of sphericity [62]. Fig. 8c shows part of a single X-ray CT cross-sectional image of the standard glass spheres embedded in epoxy. Note the particle that has a substantial amount of internal porosity, which would affect the results in laser diffraction particle size measurements since the particle would have less mass than would be expected from its outer diameter.

6.11. Shape vs. size of crushed waste glass

Waste glass is collected for recycling in the US. Crushing this glass and using it as a partial substitute for cement in concrete is a potential way to reduce the use of cement [63–65]. Measuring the particle size of this crushed material, which produces very non-spherical particles, leads to different results with different techniques. Two sieve size ranges, 25–38 μm and 63–75 μm, were studied with the combined X-ray CT and spherical harmonics method [66]. Using the 3D data from this technique, quantitative explanations were made relating the particle size as measured by sieving, laser diffraction, and X-ray CT/spherical harmonics. The shape of the particles was intimately related to the apparent size measured, not only for the laser diffraction method but also for the sieving, which were square hole wire mesh sieves. The complex geometry of the particles interacted with the simple geometry of the square wire sieves. For example, in contrast to previous findings [67], the particle width W did not necessarily give the best comparison to the sieve opening as a measure of particle size, since values of W outside the sieve ranges could be found. This was partly due to the standard deviation of the sieve openings, which allowed smaller and larger mesh openings than the average mesh opening, but also because particles with values of W larger than a square sieve opening could still pass through the sieve opening due to their non-spherical geometry. It was also shown, for these particular non-spherical particles that were randomly selected from the total particle population, how many particles were needed to get good aspect ratio (e.g. L/W, L/T) averages and distributions. Only about 30 were needed for consistent averages, but about 300 were needed for consistent aspect ratio distributions.

6.12. Particle shape for lunar soil simulant

There is ongoing research world-wide on what robotic equipment would be needed to build a lunar base. Applications such as developing robotic excavators depend on knowing the mechanical properties of the lunar regolith (soil). Since soil anywhere consists of packed particles, the mechanical properties of the soil depends sensitively on the particle shape. The lunar regolith obtained from the US Apollo missions is so scarce and precious that the amounts needed for soil mechanical analysis and testing of excavation robots are not available. NASA has developed a simulated lunar soil, denoted JSC1a [68], which has a chemical composition similar to real lunar soil and is crushed from volcanic material. Other such simulants exist and have been studied with X-ray CT techniques [14,15]. The X-ray CT/SH technique was used to characterize shape distribution of these particles for sizes (as determined by standard sieves) from about 20 μm to over 300 μm [69]. The SH coefficients for each particle were stored and can be used for future applications. Fig. 9 shows two VRML images of JSC1a particles that were larger than 300 μm.

One can extract shape parameters from the moment of inertia tensor, which is computed for all particles in the X-ray CT SH approach. The moment-of-inertia tensor is defined in the usual way [11] for every particle that was found in the epoxy matrix and which passed the error tests, and is then diagonalized to give the principal moments of inertia. These can be used in various ways to generate three orthogonal lengths that are another way of approximately defining the particle size and shape [22]. However, ratios of the diagonal elements of the moment-of-inertia tensor can be used directly as shape parameters, since for a sphere, these ratios are equal to unity. Using these parameters, one can define two independent aspect ratios for a particle in 3D using the three principal moments of inertia. In Fig. 10, the cumulative probability distribution for I_{33}/I_{22}, where $I_{33} > I_{22} > I_{11}$, in terms of volume fraction, is plotted for the four particle size classes (as defined by standard sieving) that cover the entire size range tested. These size classes were: 20–38 μm, 38–75 μm, 75–300 μm, and greater than 300 μm. The distribution of this ratio appears to be the same for all four particle size classes, which agrees, although for a narrower size range, with the results of Section 6.2.

6.13. Metal powder for additive manufacturing

Additive manufacturing (AM), which is the official name, or 3-D printing, which is the widely accepted popular name, is a method, using a number of different material technologies, to build up a

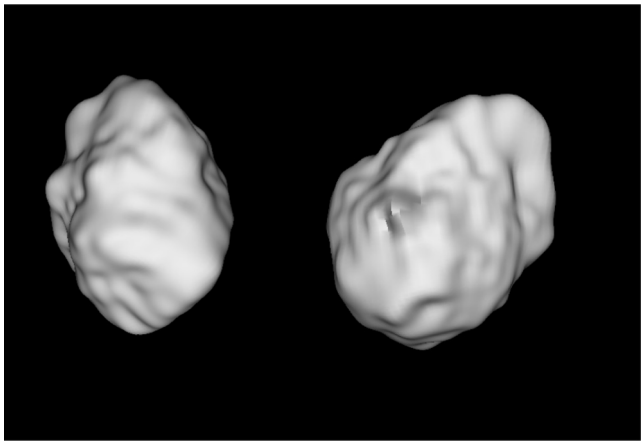

Fig. 9. VRML images of two real JSC-1A particles from the 300$^+$ size class.

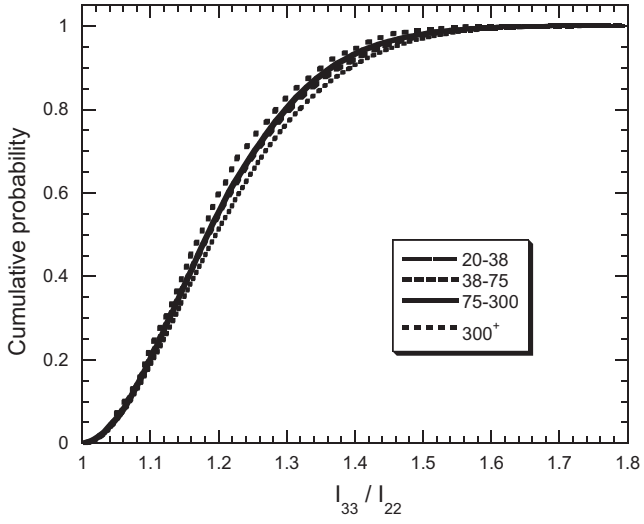

Fig. 10. The cumulative probability distribution of I_{33}/I_{22}, for the four JSC1a particle size classes considered.

part layer-by-layer. It is the opposite of the subtractive manufacturing method, which is to start with a material blank and cut or grind away all the materials that is not wanted. Michelangelo used the subtractive method in all his sculptures, where he said something like "Every block of stone has a statue inside it and it is the task of the sculptor to discover it." Direct laser sintering of metal powders is one AM method that uses a laser to melt a path in a metallic powder bed, which gradually builds up the part as the height of the powder bed increases. The shape of these metallic beads, intended to be spherical, plays an important role in how the powder is spread out for the next layer. The powder packing, which also depends on shape, can strongly affect part porosity. In this way, the powder shape can influence the quality of the final part. X-ray CT/SH techniques were used to evaluate the raw stainless steel and cobalt-chrome powder that went into an AM process [70]. Many non-spherical particles were found, as well as particles containing a small amount of internal pores.

Fig. 11 shows an SEM image of a few of the stainless steel particles used in the direct laser sintering AM process, before use. The metal powder is nominally spherical, but one can see from Fig. 11 that there are many non-sphericities, including small particles attached to larger ones and particles that are very non-spherical. An X-ray CT SH study of particle shape was made for four vials of the powder, denoted as GP1, with tens of thousands of particles examined for each vial. Fig. 12 shows the distribution of the W/T shape parameter for the four vials. Not only are the particles not spherical, but one vial is a bit different from the other three, which were all supposed to be nominally identical [70].

6.14. Effect of particle shape on particle size measurement

When one considers a sphere, the size and shape of the particle are both well-defined and independent of each other. The shape is a sphere, whose surface is a collection of points equi-distant from a central point, and the size is the length of the diameter. For an ellipsoid, the shape is tied to the length of the three semi-axes. These three lengths determine the shape. Now, how does one define the particle size? It is not well-defined as a single number, but as three numbers. For a general random star-shaped particle, size and shape are even more closely tied together. Any size measurement technique gives a result that is shape dependent. Even the results of direct measurement of a particle with a micrometer or other length measuring device depends on shape, since the length measured will be different for different ways of orienting

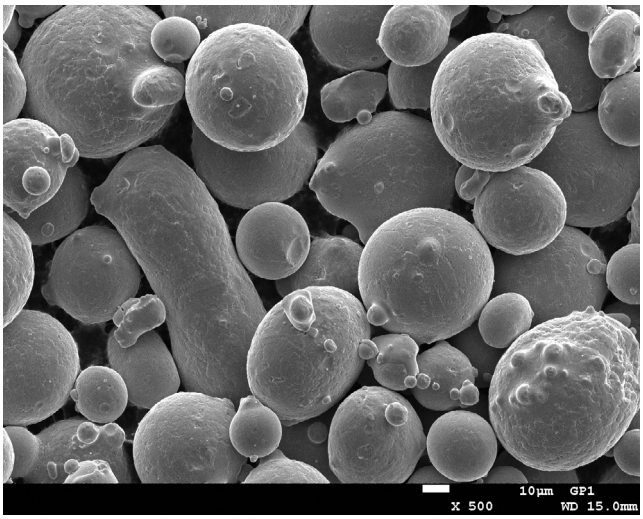

Fig. 11. Unused stainless steel powder. White bar is 10 µm long.

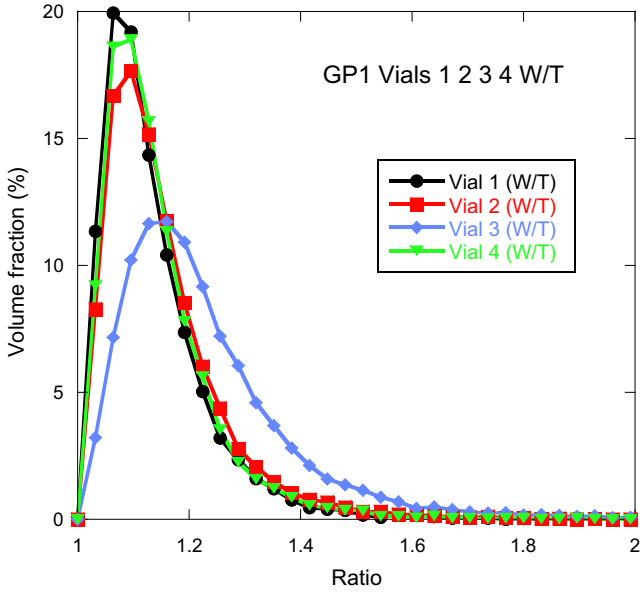

Fig. 12. The W/T ratio distribution for all four vials of virgin stainless steel powders.

the particle. For example, laser diffraction instruments interpret the diffraction pattern based on the assumption that the particles are a collection of different size spheres. Particles with the same volume, a measure of size, but a different shape will give different diffraction patterns and thus will be interpreted as different size particles. A test of these ideas was made using several rock dust sources, all under 150 µm in "size," as judged by passing through a sieve with square holes of edge length 150 µm. The particle size distribution as obtained by laser diffraction was compared with that obtained from X-ray CT/SH, which used different dimensions (e.g. L, W, T) to represent the "size" of the particles [53]. It was found that the "size" from laser diffraction most closely agreed with the length L as measured by X-ray CT/SH as discussed above. Fig. 13 illustrates this finding for one type of rock dust particle [71]. Although particle size measurement via laser diffraction was the focus of this study, it is safe to say that the particle shape will affect any particle size measurement that is being used at present, so that size and shape should not be considered, at least in an experimental view, as completely independent quantities.

6.15. Generation of new model particles based on real particles

The X-ray CT/SH method can measure many particles in one sample, but overall it is a slower process than optical methods such as laser diffraction. Therefore, it was of interest to see whether new particles could be generated, based on a sample of particles that had already been characterized with X-ray CT/SH, which would have the same shape statistics as the original sample [72,73]. A statistical method was developed to do so [72], and it was found in subsequent work that on the order of 1000 original particles were needed to be able to generate new particles that qualitatively looked like the original particles and had similar shape statistics [73]. This work will enable many new particles to be generated, based on a smaller sample of characterized particles, for model applications.

6.16. Particle shape measurement of real lunar soil

Based on the previous work with JSC1a, a lunar soil simulant [68,69], samples of two real lunar soils, one from lunar lowlands obtained during the Apollo 11 mission, and one highland soil

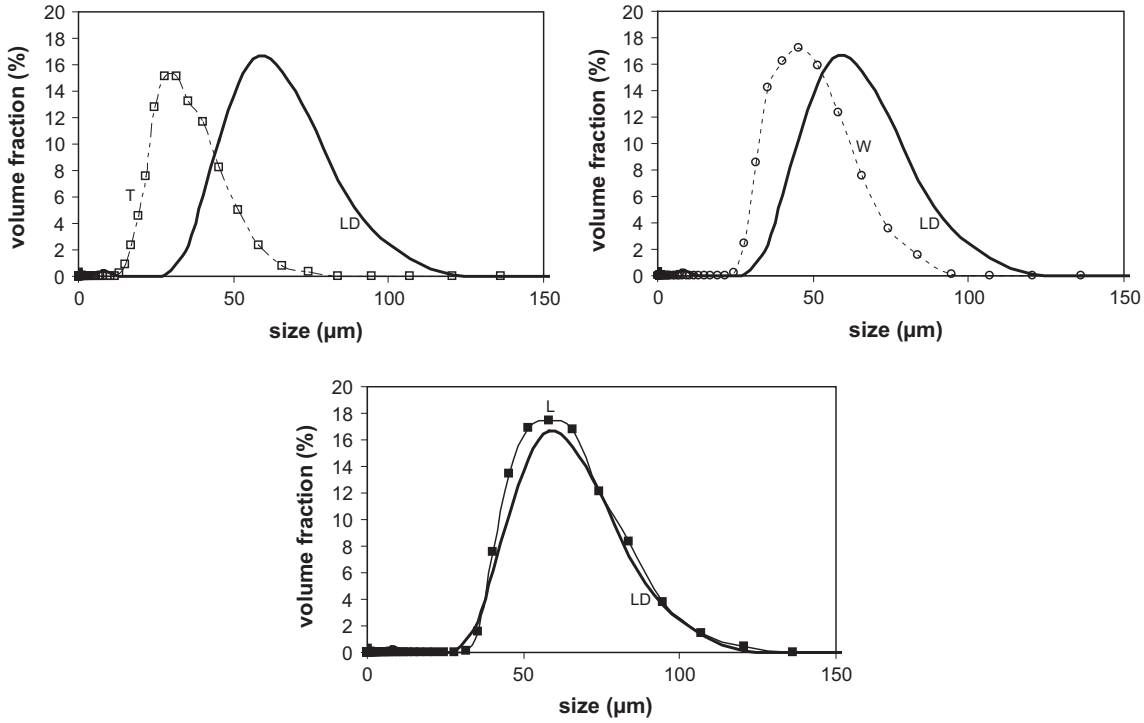

Fig. 13. Comparing the laser diffraction (LD) particle size distribution (solid lines, no data points) to that generated from X-ray CT results (data points and connecting lines) Different "size" parameters of the particles, *L*, *W*, and *T*, were used for the X-ray CT/SH results shown in the three graphs. One type of sand particle, less than 150 μm as measured by sieving, was used.

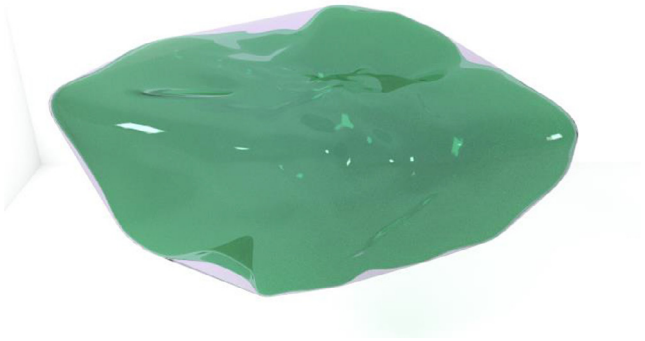

Fig. 14. 3D SH reconstruction of a coarse aggregate particle formed from blast furnace slag. The particle, rendered in green, is reconstructed by SH expansion to degree 16. The particle's convex hull is rendered in purple, and is used to compute the particle's convexity.

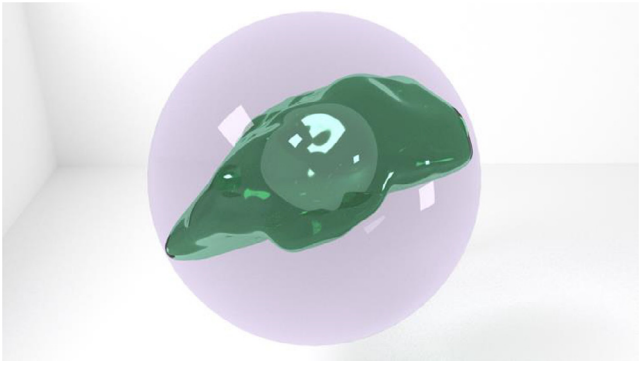

Fig. 15. 3D SH reconstruction of the same particle as in Fig. 14, rotated to a different orientation. The maximum inscribed sphere (MIS) is shown in translucent gray within the particle, and the minimum enclosing sphere (MES) is shown in purple. (For interpretation of the references to color in this figure legend, the reader is referred to the web version of this article.)

obtained during the Apollo 14 mission, were borrowed from NASA for X-ray CT/SH shape determination [74]. The ultimate goal of this work is to give analytical functions for the shapes of real lunar soil particles so that light-scattering computations can be made on them, which will enable better interpretation of measurements of sunlight scattering from lunar surfaces. This work is on-going. Other workers have previously applied X-ray CT techniques to lunar soil [12,13].

7. TSQUARE

Various algorithms for reconstructing and mathematically analyzing star shapes based on SH expansions have been collected in a software library called TSQUARE.[2] These algorithms add new capabilities to those algorithms that operate in the program part-lwt.f, previously described in Section 4.2. TSQUARE has an object-oriented structure written in C++, with extensive support from the Boost [75] and CGAL [76] libraries for applied mathematics and computational geometry, respectively, which are both peer-reviewed, open source C++ libraries. It includes the following algorithms, several of which have been described in more detail earlier in this article:

- computing SH coefficients for a shape represented as a binary digital image, and storing these SH coefficients in a text file;
- reconstructing a shape from a set of SH coefficients stored in a text file;
- filtering "ringing" artifacts (*i.e.*, Gibbs phenomenon) using either a Lanczos sigma factor [23,24] or a Hanning window [77];

[2] TSQUARE is an acronym: Toolkit for Shape QUantitative Analysis and REconstruction.

Table 1
Some shape properties calculated on particles drawn from a coarse limestone aggregate, from a fine hot asphalt aggregate, from a standard sand, and from a Portland cement powder. Shape properties are the convexity, the ratio of length to thickness (L/T), the ratio of width to thickness (W/T), the ratio of the diameter of the minimum enclosing sphere to that of the maximum inscribed sphere (BSR) and the roundness calculated using Eq. (15) [23]. (Note that all the shape properties are dimensionless.) Values reported are the mean of 200 particles, with the standard deviation enclosed in parentheses.

Source	Convexity	L/T	W/T	BSR	Roundness
Coarse limestone*	0.868	2.329	1.616	0.368	0.727
	(0.034)	(0.747)	(0.462)	(0.083)	(0.076)
Fine aggregate†	0.880	2.390	1.637	0.385	0.761
	(0.069)	(0.766)	(0.457)	(0.010)	(0.082)
Sand**	0.895	1.870	1.386	0.446	0.795
	(0.047)	(0.423)	(0.293)	(0.079)	(0.061)
Cement powder††	0.840	2.243	1.607	0.368	0.723
	(0.047)	(0.704)	(0.466)	(0.082)	(0.073)

* Coarse aggregate proficiency sample #137–#138, American Association of State Highway Transportation Officials, Washington, DC.
† Fine aggregate proficiency sample #39, American Association of State Highway Transportation Officials, Washington, DC.
** ASTM C 33 standard sand.
†† Portland cement proficiency sample #152, Cement and Concrete Reference Laboratory, Frederick, MD.

- rigid body rotation of the shape through Euler angles (α, β, γ) [78];
- calculating the volume, surface area, and volume equivalent spherical diameter (VESD);
- calculating the outward unit normal vector at any point on the surface;
- calculating the principal directions, principal curvatures, mean curvature, and Gaussian curvature at any point on the surface, including the identification of parabolic or elliptic umbilic points [79];
- computing the convex hull and the convexity, a number between zero and one defined as the volume enclosed by the particle divided by the volume enclosed by the convex hull [21,80] (see Fig. 14);
- computing the maximum inscribed sphere and minimum enclosing sphere [23]. The ratio of these two radii, denoted the bounding sphere ratio (BSR), is one measure of the particle sphericity [23] (see Fig. 15);
- computing the length (L), width (W), and thickness (T) as well as the closely-related triaxial dimensions D_1, D_2, and D_3 [23];
- computing the projected area in any direction;
- computing several different measures of sphericity, including Wadell sphericity [81], the Hofmann shape entropy [82], and the BSR value [23];
- computing two alternate measures of roundness [23,81];
- rendering the shape either as a 3D digital image or as a Virtual Reality Markup Language (VRML) file that can be viewed interactively, optionally superimposing the convex hull or bounding spheres.

The TSQUARE library can be linked to a driver program to automatically calculate shape properties of multiple particles drawn from a single population, and to report both individual results and statistics of the population. For example, Table 1 shows the mean and standard deviation of five shape characteristics calculated on 200 particles each drawn from four different sources of particles. The results of [66] showed that 200 particles were more than enough particles to compute consistent and accurate average shape parameters. The table shows that the variation in any shape characteristic within one particle source is comparable to the source-to-source variation in the mean values. This observation generally holds across a wide range of rock, sand, and cement powder sources, suggesting a degree of statistical similarity [23].

8. Summary

Within the two limits of particles that are star-shaped, and particles that are of a convenient size to be scanned rapidly in an X-ray CT, the combined X-ray CT and spherical harmonic analysis is a powerful tool for analyzing the 3D shape of particles, since it results in an analytical approximation for the full structure of a particle. Having this analytical approximation enables one to calculate essentially any shape parameter of interest. Calculations of other properties can be done using this approximation, including elastic and light scattering calculations.

Applications have been numerous. One key general finding is that particle size and shape are linked, and no measurement can treat these as separate variables for all particles that are not spheres. Another important general finding is that, for blasting, crushing, and ball-mill grinding processes, the particle shape tends to stay nearly the same, statistically, over wide particle size ranges for a given material type. Specifically, knowing the detailed 3D particle shape statistics can be of great assistance in many applications, including particle reactivity, formation of biofilms on particles, and the rheology of dense suspensions. It is hoped that perusal of the review article and the more specific article referenced herein will prove useful to powder science and technology researchers, and especially those in the early stage of their careers.

References

[1] E.J. Garboczi, J.F. Douglas, Intrinsic conductivity of objects having arbitrary shape and conductivity, Phys. Rev. E 53 (1996) 6169–6180.
[2] M.L. Mansfield, J.F. Douglas, E.J. Garboczi, Intrinsic viscosity and the electrical polarizability of arbitrarily shaped objects, Phys. Rev. E 64 (2001) 61401–61416.
[3] D.J. Audus, A.M. Hassan, E.J. Garboczi, S.D. Hudson, J.F. Douglas, Interplay of particle shape and suspension properties: a study of cube-like particles, Soft Matter 11 (2015) 3360–3366, http://dx.doi.org/10.1039/C45SM02869D.
[4] E.J. Garboczi, K.A. Snyder, J.F. Douglas, M.F. Thorpe, Geometrical percolation threshold of overlapping ellipsoids, Phys. Rev. E 52 (1995) 819–828.
[5] S. Meille, E.J. Garboczi, Linear elastic properties of 2-D and 3-D models of porous materials made from elongated objects, Mod. Simulat. Mater. Sci. Eng. 9 (2001) 1–20.
[6] James R. Munkres, Topology, second ed., Prentice Hall, 2000, ISBN 0-13-181629-2.
[7] C.R. Smith, A characterization of star-shaped sets, Am. Math. Month. 75 (1968) 386;
H. Brunn, Über Kerngebiete, Math. Ann. 73 (1913) 436–440.
[8] S.T. Erdoğan, P.N. Quiroga, D.W. Fowler, H.A. Saleh, R.A. Livingston, E.J. Garboczi, P.M. Ketcham, J.G. Hagedorn, S.G. Satterfield, Three-dimensional shape analysis of coarse aggregates: new techniques for and preliminary results on several different coarse aggregates and reference rocks, Cem. Concr. Res. 36 (2006) 1619–1627.
[9] H. Yu, G. Cao, L. Burk, Y. Lee, J. Lu, P. Santago, O. Zhou, G. Wang, Compressive sampling based interior reconstruction for dynamic carbon nanotube micro-CT, J. X-Ray Sci. Technol. 17 (2009) 295–303, http://dx.doi.org/10.3233/XST-2009-0230.
[10] S. Cho, J. Bian, C.A. Pelizzari, C.T. Chen, T.C. He, X. Pan, Region-of-interest image reconstruction in circular cone-beam microCT, Med. Phys. 34 (2007) 4923–4933, http://dx.doi.org/10.1118/1.2804924.
[11] E.J. Garboczi, Three-dimensional mathematical analysis of particle shape using X-ray tomography and spherical harmonics: application to aggregates used in concrete, Cem. Concr. Res. 32 (2002) 1621–1638.

[12] J. Katagiri, T. Matsushima, Y. Yamada, Statistics on 3D particle shapes of lunar soil (no. 60501) obtained by micro X-Ray CT and its image-based DEM simulation, Earth Space 2010 (2010) 254–259, http://dx.doi.org/10.1061/41096(366)26 (ASCE Proceedings).
[13] J. Katagiri, T. Matsushima, Y. Yamada, A. Tsuchiyama, T. Nakano, K. Uesugi, M. Ohtake, K. Saiki, Investigation of 3D grain shape characteristics of lunar soil retrieved in Apollo 16 using image-based discrete-element modeling, J. Aerosp. Eng. (2014) 04014092-1–04014092-13, http://dx.doi.org/10.1061/(ASCE)AS.1943-5525.0000421.
[14] T. Matsushima, J. Katagiri, K. Uesugi, A. Tsuchiyama, T. Nakano, 3D shape characterization and image-based DEM simulation of the lunar soil simulation FJS-1, J. Aerosp. Eng. 22 (2009) 15–23, http://dx.doi.org/10.1061/(ASCE)0893-1321(2009)22:1(15).
[15] T. Matsushima, J. Katagiri, K. Uesugi, A. Tsuchiyama, T. Nakano, Image-based modeling of lunar soil simulant for 3-D DEM simulations, Earth Space (2006) 1–8, http://dx.doi.org/10.1061/40830(188)23 (ASCE Proceedings).
[16] G. Arfken, Mathematical Methods for Physicists, second ed., Academic Press, New York, 1970.
[17] <http://wiht.link/VRMLanguage> (active link as of October 3, 2016).
[18] M.D. Buhmann, Radial Basis Functions: Theory and Implementations, Cambridge University Press, Cambridge, 2003.
[19] J.C. Carr, W.R. Fright, R.K. Beatson, Surface interpolation with radial basis functions for medical imaging, IEEE Trans. Med. Imaging 16 (1997) 96–107.
[20] J.C. Carr, R.K. Beatson, J.B. Cherrie, T.J. Mitchell, W.R. Fright, B.C. McCallum, T.R. Evans, in: SIGGRAPH'01 Proceedings of the 28th Annual Conference on COMPUTER GRAPHICS and Interactive Techniques, ACM, New York, NY, USA, 2001, pp. 67–76, http://dx.doi.org/10.1145/383259.383266, ISBN:1-58113-374-X.
[21] E.J. Garboczi, J.W. Bullard, Contact function, uniform-thickness shell volume, and convexity measure for 3D star-shaped random particles, Powder Technol. 237 (2013) 191–201, http://dx.doi.org/10.1016/j.powtec.2013.01.019.
[22] M.A. Taylor, E.J. Garboczi, S.T. Erdoğan, D.W. Fowler, Some properties of irregular particles in 3-D, Powder Technol. 162 (2006) 1–15.
[23] J.W. Bullard, E.J. Garboczi, Defining shape measures for 3D star-shaped particles: sphericity, roundness, and dimensions, Powder Technol. 249 (2013) 241–252.
[24] C. Lanczos, Applied Analysis, Prentice Hall, Englewood Cliffs, NJ, 1956.
[25] G.S. Cheok, W.C. Stone, E.J. Garboczi, Using LADAR to characterize the 3-D shape of aggregates: preliminary results, Cem. Concr. Res. 36 (2006) 1072–1075.
[26] Z. Qian, E.J. Garboczi, G. Ye, E. Schlangen, Anm: a geometrical model for the composite structure of mortar and concrete using real-shape particles, to be published, Mater. Struct. (2015).
[27] D. Weaire, T. Aste, The Pursuit of Perfect Packing, CRC Press, Boca Raton, Florida, 2000.
[28] C. O'Sullivan, Particulate Discrete Element Modelling: A Geomechanics Perspective, Spon Press, London, 2011.
[29] J.W. Perram, M.S. Wertheim, Statistical mechanics of hard ellipsoids. I. Overlap algorithm and the contact function, J. Comput. Phys. 58 (1985) 409–441;
J. Vieillard-Baron, Phase transitions of the classical hard-ellipse system, J. Chem. Phys. 56 (1972) 4729–4738.
[30] D.P. Bentz, J.T.G. Hwang, C. Hagwood, E.J. Garboczi, K.A. Snyder, N. Buenfeld, K. L. Scrivener, Interfacial zone percolation in concrete: effects of interfacial zone thickness and aggregate shape, MRS Symposium Proceedings, 370, 1995, pp. 437–442, Found at: <https://concrete.nist.gov/garbocz/paper72/paper72.html>.
[31] Z. Qian, E.J. Garboczi, G. Ye, E. Schlangen, Anm: a geometrical model for the composite structure of mortar and concrete using real-shape particles, Mater. Struct. 49 (2015) 149–158, http://dx.doi.org/10.1617/s11527-014-0482-5.
[32] Y. Lu, E.J. Garboczi, Bridging the gap between random microstructure and 3D meshing, J. Comput. Civ. Eng. (2012), http://dx.doi.org/10.1061/(ASCE)CP.1943-5487.0000270.
[33] Stephen Thomas, Yang Lu, E.J. Garboczi, Improved model for 3-D virtual concrete: Anm model, ASCE J. Comput. Civ. Eng. 30 (2015), http://dx.doi.org/10.1061/(ASCE)CP.1943-5487.0000494, 04015027.
[34] Stephen Thomas, Yang Lu, E.J. Garboczi, Application of Anm model to generate and analyze interfacial transition zone microstructure in realistic virtual mortar samples, 2016 (in preparation).
[35] D.P. Bentz, E. Schlangen, E.J. Garboczi, Computer simulation of interfacial zone microstructure and its effect on the properties of cement-based materials, in: Jan Skalny, Sidney Mindess (Eds.), Materials Science of Concrete IV, American Ceramic Society, Westerville, Ohio, 1995.
[36] D.P. Bentz, E.J. Garboczi, J.W. Bullard, C.F. Ferraris, N.S. Martys, Virtual testing of cement and concrete, in: Joseph Lamond, James Pielert (Eds.), Significance of Tests and Properties of Concrete and Concrete-Making Materials, ASTM STP 169D, 2006;
J.I. Bhatty, F.M. Miller, S.H. Kosmatka (Eds.), Innovations in Portland Cement Manufacturing, Portland Cement Association, Skokie, IL 60077, 2004, pp. 1311–1331.
[37] J.F. Douglas, E.J. Garboczi, Intrinsic viscosity and polarizability of particles having a wide range of shapes, Adv. Chem. Phys. 91 (1995) 85–153.
[38] E.J. Garboczi, J.F. Douglas, R.B. Bohn, A hybrid finite element-analytical method for determining the intrinsic elastic moduli of particles having moderately extended shapes and a wide range of elastic properties, Mech. Mater. 38 (2006) 786–800;
E.J. Garboczi, J.F. Douglas, Elastic moduli of composites containing a low concentration of complex-shaped particles having a general property contrast with the matrix, Mech. Mater. 51 (2012) 53–65.
[39] Feng Zhang, Bin Ye, Guanlin Ye, A unified description of Toyoura sand, in: Qiang Yang, Jian-Min Zhang, Hong Zheng, Yangping Yao (Eds.), Constitutive Modeling of Geomaterials: Advances and New Applications, Springer Series in Geomechanics and Geoengineering, 2013, ISBN: 978-3-642-32813-8.
[40] British Geological Survey, <https://www.bgs.ac.uk/>.
[41] E.J. Garboczi, X. Liu, M.A. Taylor, The shape of a blasted and crushed rock material over more than three orders of magnitude: 20 mm to 60 mm, Powder Technol. 229 (2012) 84–89, http://dx.doi.org/10.1016/j.powtec.2012.06.012.
[42] A. Gray, Modern Differential Geometry of Curves and Surfaces, CRC Press, Florida, 1993.
[43] J. Serra, Image Analysis and Mathematical Morphology, Academic Press, New York, 1982.
[44] Thomas Fletcher, Chandan Chandan, Eyad Masad, Krishna Sivakumar, Aggregate imaging system for characterizing the shape of fine and coarse aggregates, Trans. Res. Record: J. Trans. Res. Bd. 1832, paper no. 03-2174 (2003). http://dx.doi.org/10.3141/1832-09.
[45] Eyad Masad, Shadi Saadeh, Taleb Al-Rousan, Edward Garboczi, Dallas Little, Computations of particle surface characteristics using optical and X-ray CT images, Comput. Mater. Sci. 34 (2005) 406–424.
[46] Enad Mahmoud, Leslie Gates, Eyad Masad, Edward Garboczi, Comprehensive evaluation of AIMS texture, angularity, and dimensions measurements, J. Mater. Civ. Eng. 22 (2010) 369–379.
[47] Rolands Cepuritis, Edward J. Garboczi, Stefan Jacobsen, Comparison of 2D and 3D shape results for concrete aggregate fines produced by VSI crushing, Powder Technol. (2016) (in press).
[48] E.J. Garboczi, J.W. Bullard, Measuring the three-dimensional shape of sand particles, draft standard for ASTM Committee D04.51 Aggregate Tests.
[49] Rolands Cepuritis, B.J. Wigum, E.J. Garboczi, Ernst Mørtsell, Stefan Jacobsen, Filler from crushed aggregate for concrete: pore structure, specific surface, particle shape and size distribution, Cem. Concr. Compos. 54 (2014) 2–16, http://dx.doi.org/10.1016/j.cemconcomp.2014.03.010.
[50] R. Cepuritis, E.J. Garboczi, C.F. Ferraris, S. Jacobsen, B.E. Sørensen, Measurement of particle size distribution and specific surface area for crushed concrete aggregate, Adv. Powder Technol. (2016) (in press).
[51] Rolands Cepuritis, Edward J. Garboczi, Stefan Jacobsen, Three dimensional shape analysis of concrete aggregate fines produced by VSI crushing, Powder Technol. (2016) (in press).
[52] J. Rodriguez, T. Edeskär, S. Knutsson, Particle shape quantities and measurement techniques – a review, Electron. J. Geotech. Eng. 18 (2013) 169–198.
[53] European Committee for Standardization, EN 933-3:2012 Tests for Geometrical Properties of Aggregates – Part 3: Determination of Particle Shape – Flakiness Index, CEN, Brussels, 2012.
[54] U.S. Geological Survey, <http://minerals.usgs.gov/minerals/pubs/commodity/cement/mcs-2016-cemen.pdf>.
[55] E.J. Garboczi, J.W. Bullard, Shape analysis of a reference cement, Cem. Concr. Res. 34 (2004) 1933–1937.
[56] S.T. Erdoğan, X. Nie, P.E. Stutzman, E.J. Garboczi, Micrometer-scale 3-D imaging of eight cements: particle shape, cement chemistry, and the effect of particle shape on laser diffraction size analysis, Cem. Concr. Res. 40 (2010) 731–739.
[57] Lorenz Holzer, Robert Flatt, S.T. Erdoğan, X. Nie, E.J. Garboczi, Shape comparison between 0.4 μm to 2.0 μm and 20 μm to 60 μm cement particles, J. Am. Ceram. Soc. 93 (2010) 1626–1633.
[58] J.W. Bullard, E.J. Garboczi, A model investigation of the influence of particle shape on Portland cement hydration, Cem. Concr. Res. 36 (2006) 1007–1015.
[59] T.C. Zhang, P. Bishop, Density, porosity, and pore structure of biofilms, Water Res. 28 (11) (1994) 2267–2277.
[60] H. Shin, K. Yoo, J. Park, Removal of polychlorinated phenols in sequential anaerobic-aerobic biofilm reactors packed with tire chips, Water Environ. Res. 71 (1999) 363–367.
[61] M. Hu, T. Zhang, J. Stansbury, J. Neal, E.J. Garboczi, Determination of porosity and thickness of biofilm attached on irregular-shaped media, J. Environ. Eng. 139 (7) (2013) 923–931.
[62] E.J. Garboczi, H. Azari, Evaluating particle sphericity: a comparison of mechanical, 2D optical, and 3D X-ray computed tomography methods applied to standard reference glass beads and glass beads used in pavement marking paint, 2016 (in preparation).
[63] M. Mirzahosseini, K.A. Riding, Influence of different particle sizes on reactivity of finely ground glass as supplementary cementitious materials (SCM), Cem. Concr. Compos. 56 (2015) 95–105.
[64] C. Meyer, Recycled glass – from waste material to valuable resource, in: Int. Symposium on recycling and reuse of glass cullet, University of Dundee, Scotland, 2001, pp. 1–10.
[65] A.C.P. Galvao, A.C.M. Farias, J.U.I. Mendes, Characterization of waste of soda-lime glass generated from lapping process to reuse as filler in composite materials as thermal insulation, Ceramica 61 (2015) 367–373.
[66] E.J. Garboczi, K.A. Riding, Mohammadreza Mirzahosseini, Particle shape effects on particle size measurement for crushed waste glass, Powder Technol. (2016) (in press).
[67] J.M.R. Fernlund, The effect of particle form on sieve analysis: a test by image analysis, Eng. Geol. 50 (1) (1998) 111–124.
[68] D.S. McKay, J.L. Carter, W.W. Boles, C.C. Allen, J.H. Alton, JSC-1: a new lunar soil simulant, in: Engineering, Construction, and Operations in Space IV, ASCE, New

York, pp. 857–866. <http://isru.msfc.nasa.gov/lib/Documents/JSC-1A_Bulk_Data_Characterization_draft.pdf>.
[69] E.J. Garboczi, Three dimensional shape analysis of JSC-1A simulated lunar regolith particles, Powder Technol. 207 (2011) 96–103.
[70] J.A. Slotwinski, E.J. Garboczi, P.E. Stutzman, C.F. Ferraris, S.S. Watson, M.A. Peltz, Characterization of metal powders used for additive manufacturing, J. Res. Nat. Inst. Stand. Technol. 119 (2014), http://dx.doi.org/10.6028/jres.119.018.
[71] S.T. Erdoğan, D.W. Fowler, E.J. Garboczi, Shape and size of microfine aggregates: X-ray microcomputed tomography vs. laser diffraction, Powder Technol. 177 (2007) 53–63.
[72] M. Grigoriu, E.J. Garboczi, C. Kafali, Spherical harmonic-based random fields for aggregates used in concrete, Powder Technol. 166 (2006) 123–138.
[73] X. Liu, E.J. Garboczi, M. Grigoriu, Y. Lu, S.T. Erdoğan, Spherical harmonic-based random fields based on real particle 3D data: improved numerical algorithm and quantitative comparison to real particles, Powder Technol. 207 (2011) 78–86.
[74] T. Lafarge, A. Possolo, E.J. Garboczi, A. Debay, J. Guogen, A. Curtin, O. Munoz, Three-dimensional shape characterization of lunar regolith from the Apollo 11 and Apollo 14 missions, 2016 (in preparation).
[75] Boost source code libraries available at <http://www.boost.org> (last accessed on June 11, 2015).
[76] Computational Geometry Algorithms Library (CGAL) binary and source code libraries available at <www.cga.org> (last accessed on June 11, 2015).
[77] P.-P. Sloan, Stupid spherical hamonics (SH) tricks, in: Game Developers Conference, San Francisco, CA, UBM Tech Web Game Network, 2008. <http://www.ppsloan.org/publications/StupidSH36.pdf> (last accessed on June 11, 2015).
[78] Z. Gimbutas, L. Greengard, A fast and stable method for rotating spherical harmonic expansion, J. Comput. Phys. 228 (2009) 5621–5627.
[79] E. Kreyszig, Differential Geometry, Mathematical Expositions Series, vol. 11, University of Toronto Press, Ontario, Canada, 1959.
[80] P.L. Rosin, C.L. Mumford, A symmetric convexity measure, Comput. Vis. Image Underst. 103 (2006) 101–111.
[81] H. Wadell, Volume, shape, and roundness of rock particles, J. Geol. 40 (1932) 443–451.
[82] H.J. Hofmann, Grain-shape indices and isometric graphs, J. Sediment. Res. A 64 (1994) 916–920.